The Astrophysical Journal, 649:224–234, 2006 September 20

SYNTHESIS IMAGING OF DENSE MOLECULAR GAS IN THE N113 H II REGION OF THE LARGE MAGELLANIC CLOUD

Tony Wong,[1] John B. Whiteoak, and Jürgen Ott
CSIRO Australia Telescope National Facility, P.O. Box 76, Epping, NSW 1710, Australia; tony.wong@csiro.au

Yi-nan Chin
Department of Physics, Tamkang University, 25137 Tamsui, Taipei, Taiwan

and

Maria R. Cunningham
School of Physics, University of New South Wales, Sydney, NSW 2052, Australia
Received 2005 December 16; accepted 2006 April 6

ABSTRACT

We present aperture synthesis imaging of dense molecular gas in the Large Magellanic Cloud, taken with the prototype millimeter receivers of the Australia Telescope Compact Array (ATCA). Our observations of the N113 H II region reveal a condensation with a size of $\sim 6''$ (1.5 pc) FWHM, detected strongly in the 1–0 lines of HCO^+, HCN, and HNC, and weakly in C_2H. Comparison of the ATCA observations with single-dish maps from the Mopra Telescope and sensitive spectra from the Swedish-ESO Submillimetre Telescope indicates that the condensation is a massive clump of $\sim 10^4\ M_\odot$ within a larger $\sim 10^5\ M_\odot$ molecular cloud. The clump is centered adjacent to a compact, obscured H II region that is part of a linear structure of radio continuum sources extending across the molecular cloud. We suggest that the clump represents a possible site for triggered star formation. Examining the integrated line intensities as a function of interferometer baseline length, we find evidence for decreasing HCO^+/HCN and HCN/HNC ratios on longer baselines. These trends are consistent with a significant component of the HCO^+ emission arising in an extended clump envelope and a lower HCN/HNC abundance ratio in dense cores.

Subject headings: galaxies: ISM — ISM: molecules — ISM: structure — Magellanic Clouds

1. INTRODUCTION

Cold molecular gas in the interstellar medium (ISM) is usually studied via rotational transitions of trace molecules that emit at millimeter and submillimeter wavelengths. The most commonly used tracer is CO, which typically traces gas densities of $\sim 10^2$–10^3 cm^{-3}. Higher densities are best probed using molecules with larger dipole moments, such as HCO^+ and HCN. Emission from these molecules comes from the densest condensations within molecular clouds, often referred to as "clumps" and "cores" (e.g., Blitz 1991). A molecular core has typical radius $R \sim 0.1$ pc, mass $M \sim 1$–$10\ M_\odot$, and density $n \gtrsim 10^4$ cm^{-3} and is thought to eventually form a single-star or multiple-star system. Clumps are somewhat larger structures that may evolve into star clusters. The use of high-density tracers to study the initial conditions for star formation has long been common practice for Galactic observers and has recently gained greater prominence in studies of nearby galaxies following the demonstration of a tight correlation between HCN and far-infrared (FIR) luminosities (Gao & Solomon 2004a), the latter tracing recent star formation.

Although they have similar dipole moments, HCO^+ and HCN may not trace dense gas equally well, as one must consider the chemical processes that lead to their formation and destruction. This becomes especially apparent when examining molecular abundances in the Magellanic Clouds, where a lower dust-to-gas ratio and locally active star formation activity combine to yield a stronger photoionizing flux than in the Galaxy. As a result, molecular clouds are immersed in extensive photon-dominated regions (PDRs) where carbon is mostly ionized, as evidenced by the much higher [C II]/CO intensity ratios in the LMC (Mochizuki et al. 1994; Israel et al. 1996). While the formation of HCO^+ in regions shielded from far-ultraviolet (FUV) radiation is dominated by reactions between H_3^+ and CO, it can also occur in PDRs via reactions between C^+ and OH, O_2, and H_2O (Graedel et al. 1982). Thus, the spatial extent of the HCO^+ emission may be much larger than that of HCN, even comparable to that of CO.

The HNC molecule, on the other hand, has been suggested to be a tracer of cold cores, as steady state chemical models predict that it will be much weaker than HCN in regions of high temperature and density (Schilke et al. 1992). Consistent with these predictions, the HCN/HNC abundance ratio is particularly high ($\approx$80) in the hot core of Orion KL (Schilke et al. 1992), whereas it is close to unity in cool dark clouds (Churchwell et al. 1984; Hirota et al. 1998). However, observations of starburst galaxies, where temperatures are expected to be high, have revealed HNC intensities that are sometimes close to those of HCN (Huettemeister et al. 1995; Aalto et al. 2002). While an extended component of cool, quiescent gas could contribute to the HNC emission, Aalto et al. (2002) speculate that PDR chemistry may play a role; reactions involving $HCNH^+$ may become important, which recombines to produce HCN and HNC with equal probability and largely independent of kinetic temperature. Thus, HNC is potentially another tracer of PDR conditions.

As one of the initial targets for the prototype millimeter receivers on the Australia Telescope Compact Array[2] (ATCA), we

[1] Also at School of Physics, University of New South Wales, Sydney, NSW 2052, Australia.

[2] The Australia Telescope is funded by the Commonwealth of Australia for operation as a National Facility managed by CSIRO.

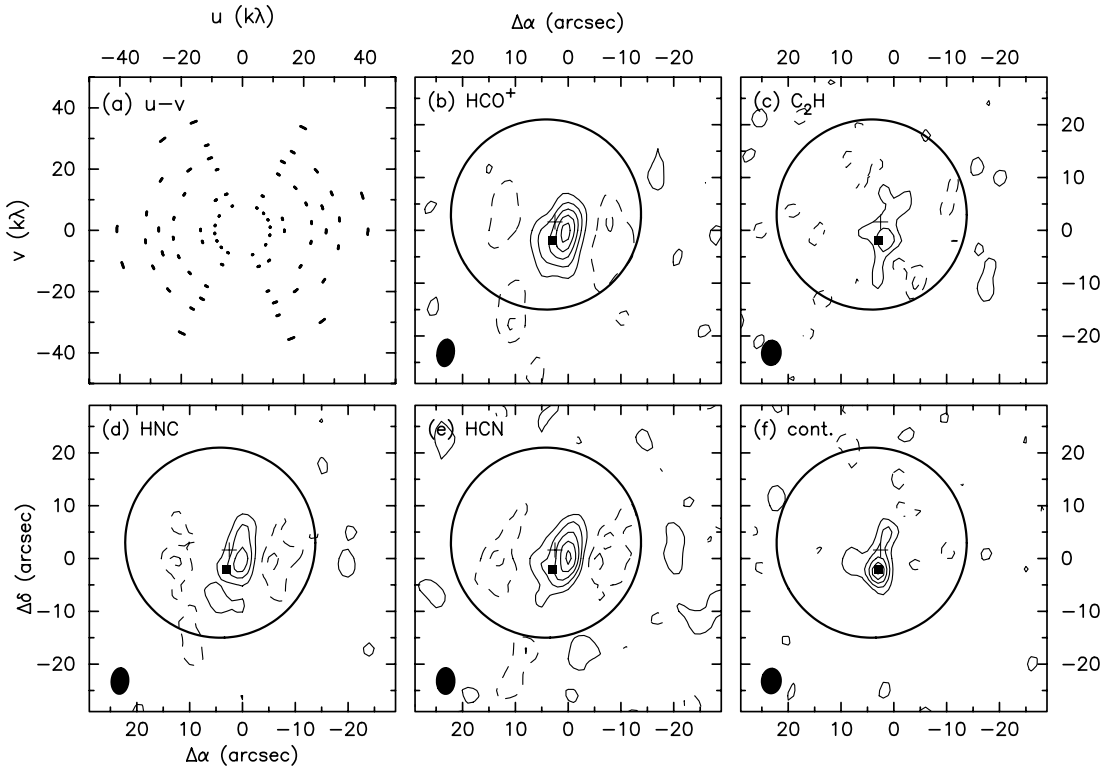

FIG. 1.—Summary of ATCA observations toward N113. (*a*) Coverage of the visibility plane for HCO^+ obtained from combining both runs. Other panels show integrated intensity maps for (*b*) HCO^+, (*c*) C_2H, (*d*) HNC, (*e*) HCN, and (*f*) continuum. Offsets are relative to $\alpha_{J2000.0} = 5^h13^m17^s.2$, $\delta_{J2000.0} = -69°22'23''$. The synthesized beam FWHM is shown in the bottom left corner, and the large circle represents the FWHM field of view. The filled square and plus sign represent the positions of the *K*-band source and the weaker H_2O maser, respectively. The contour levels are spaced by 6 K km s^{-1} for HCO^+ and HCN, 3 K km s^{-1} for HNC and C_2H, and 0.06 K for the continuum.

have observed the H II region N113 in the Large Magellanic Cloud (LMC) in the 3 mm transitions of HCO^+, HCN, HNC, and C_2H. The LMC's proximity ($d = 52$ kpc; Panagia 1999) and low metallicity make it a very attractive target for studies of the molecular ISM, but its southern declination has heretofore made it inaccessible to millimeter interferometry. We use HCN as a fiducial dense gas tracer and examine the relative intensities of the other molecular lines (including C_2H, produced in reactions involving C^+) for enhancements due to the presence of a PDR. In particular, we examine the line ratios as a function of spatial scale, which allows a comparison of compact and extended emission regions.

The molecular cloud associated with N113 (Henize 1956) is one of the richest in the LMC, with a peak CO (1–0) brightness temperature (measured with the 45″ beam of the Swedish-ESO Submillimetre Telescope [SEST]) of ~9 K (Chin et al. 1997). Three young (<10 Myr) stellar clusters, NGC 1874, NGC 1876, and NGC 1877 (Bica et al. 1992), are also associated with N113. Current star formation activity appears concentrated in three compact radio continuum sources, superposed on an extended emission component and aligned in a northwest–southeast direction with separations of ~20″ (Brooks & Whiteoak 1997). The faintest, easternmost source contains by far the brightest H_2O maser in the LMC (Whiteoak & Gardner 1986; Lazendic et al. 2002), as well as an OH maser (Brooks & Whiteoak 1997). The brightest, westernmost source also shows H_2O maser emission (Lazendic et al. 2002); it is toward this source that we have targeted our ATCA observations. All four of the 3 mm transitions observed with ATCA have been previously detected in this region with the SEST. In this paper we present the ATCA results and compare them with single-dish results from the Mopra and SEST telescopes.

2. OBSERVATIONS

2.1. *ATCA* 3 mm *Data*

Observations with the ATCA were made in 2003 July and August in the EW214 and EW367 configurations, respectively. At the time of the observations, the ATCA had three antennas of 22 m diameter equipped with dual polarization 3 mm receivers covering the bands 84.9–87.3 and 88.5–91.3 GHz. At these frequencies the primary beam has a FWHM of 36″. Both configurations had all three antennas arranged in an east–west line. The EW214 configuration provided baselines of 30, 75, and 105 m, whereas the EW367 provided baselines of 45, 90, and 135 m. The pointing center for the observations was $\alpha_{J2000.0} = 5^h13^m18^s$, $\delta_{J2000.0} = -69°22'20''$. The ATCA correlator can be configured to observe two frequencies simultaneously, and we cycled between three pairs of frequencies during each observing session in order to obtain comparable coverage of the visibility plane. The first pair of frequencies consisted of the HCO^+ ($J = 1$–0) and HNC ($J = 1$–0) lines at 89.1885 and 90.6635 GHz, respectively, redshifted to the appropriate observatory frequency for $v_{LSR} = 235$ km s^{-1}, the second pair consisted of the HCN ($J = 1$–0) line at 88.6318 GHz and HNC, and the third pair consisted of the C_2H ($N = 1$–0, $J = 3/2$–1/2, $F = 2$–1) line at 87.3169 GHz and a 128 MHz wide continuum window at 86.243 GHz. Each line was observed with a channel spacing of 0.5 MHz across a 64 MHz bandwidth, except for C_2H, which was observed with a channel spacing of 0.0625 MHz across 16 MHz. Figure 1*a*

TABLE 1
PROPERTIES OF THE ATCA IMAGES

Line	Beam Size (arcsec)	Beam P.A. (deg)	σ_{ch}[a] (mJy beam^{-1})	σ_{ch} (K)	T_{peak} (K)	Velocity range (km s^{-1})	Flux[b] (Jy km s^{-1})
HCO^+	5.1×3.2	-9	41	0.38	4.2	[229, 241]	5.2–8.8
HCN	5.0×3.4	0	42	0.39	2.8	[223, 243]	4.1–6.9
HNC	4.9×3.3	-5	23	0.21	1.4	[229, 241]	1.0–2.1
C_2H.....	4.7×3.6	-5	49	0.46	1.1	[233, 239]	0.5–1.5
Cont.....	4.7×3.7	-4	3	0.03	0.3	...	0.04[c]

[a] The rms noise for a 2 km s^{-1} channel (line images) or continuum integrated across 84 MHz.
[b] Flux measurements are made in boxes of $10'' \times 10''$ and $20'' \times 20''$ centered on $\alpha_{J2000.0} = 5^h13^m17^s.2$, $\delta_{J2000.0} = -69^\circ22'23''$.
[c] Continuum value in units of jansky.

shows the coverage of the visibility plane obtained for the HCO^+ line.

The data were calibrated and imaged with the MIRIAD package (Sault et al. 1995), which at ATNF has been updated with new procedures to handle ATCA 3 mm data. Flux calibration was performed using Uranus, while the quasars B0537−441 and B1253−055 (3C 279) were used for gain and bandpass calibration, respectively. However, for the last frequency pair (C_2H and continuum) the SiO maser R Dor was used for gain calibration instead; in doing so the maser flux was assumed to be constant over the course of an ∼8 hr observation. An instrumental phase error causing phase discontinuities when changing sources had been identified with ATCA 3 mm data,[3] and we compensated for this using an antenna position correction that was determined by observations of multiple quasars within a few days of the observations. We produced channel maps spaced in velocity by 2 km s^{-1}, which is close to the effective resolution provided by the correlator in the HCN, HNC, and HCO^+ lines. The phase center was shifted to $\alpha_{J2000.0} = 5^h13^m17^s.2$, $\delta_{J2000.0} = -69^\circ22'23''$ before imaging, a shift of 5″ (this shift has negligible impact on the primary beam response at the locations of detected emission). The noise level and synthesized beamwidth for each map are given in Table 1. After imaging the maps were CLEANed to a 2 σ level.

2.2. *ATCA* 1.3 cm *Data*

Additional observations were obtained with ATCA in 2005 March using the recently installed 12 mm receivers. N113 was observed in the H214 configuration (baseline lengths 80–250 m) over 2 days with a total integration time of 160 minutes. The correlator was configured for 512 channels across 8 MHz (velocity resolution 0.24 km s^{-1}) at 23.673 GHz and 32 channels across 128 MHz at 23.9 GHz. The narrowband observations were designed to detect the $NH_3(1, 1)$ transition but failed to do so at an rms noise level of 20 mJy beam^{-1}. The wideband observations, used to image the continuum, achieved a noise level of ∼0.4 mJy beam^{-1}. Flux, bandpass, and phase calibration were performed using the quasars B1934−638, B1921−293, and B0454−810, respectively, following standard reduction procedures in MIRIAD. After Fourier inversion the 1.3 cm continuum image was CLEANed and restored using a beam size of $10''.1 \times 9''.1$. Note that because of the limited coverage of the Fourier plane achieved with the H214 configuration, structure on scales much larger than 30″ will be poorly imaged. Thus, the resulting image is dominated by compact ionized regions, and the extended continuum emission from the large-scale H II region was not detected.

[3] This is believed to be an instrumental error that corrupts the antenna baseline solution.

2.3. *SEST Data*

Although most of our comparison with SEST data makes use of values previously presented by Chin et al. (1997), we also made use of some data that had not yet been published. These consisted of small grid maps made in the HCN ($J = 1 \rightarrow 0$) and HCO^+ ($J = 1 \rightarrow 0$) lines in two observing runs with the SEST in 1997 January and July. The maps cover a region of roughly $1'.5 \times 1'.5$ centered on the position $\alpha_{J2000.0} = 5^h13^m18^s.2$, $\delta_{J2000.0} = -69^\circ22'35''$. The grid spacing was 20″ (for comparison the SEST beam has a FWHM of 58″), but the grids were not completely sampled in the outer parts. A 3 mm SIS receiver was used in single-sideband mode with a 2000 channel acousto-optical spectrometer having a 43 kHz channel separation.

A dual beam switching mode, in which the source is placed alternately in the main and reference beams, was used to remove the sky background, and the spectra were placed on a T_{MB} scale using a main beam efficiency of 0.76. Typical single-sideband (SSB) system temperatures were ∼200 K. The CLASS package was used to calibrate and baseline the spectra. For purposes of this paper, we have produced high signal-to-noise ratio spectra for both lines by averaging the nine spectra within $-20'' < \Delta\alpha < 20''$ and $-20'' < \Delta\delta < 20''$ relative to the center position. The corresponding maps show only a moderately resolved central source and are not reproduced here. Further details of the SEST observations will be presented in a forthcoming paper (M. Wang et al. 2006, in preparation).

2.4. *Mopra Data*

A $4' \times 4'$ region centered on the position $\alpha_{J2000.0} = 5^h13^m18^s$, $\delta_{J2000.0} = -69^\circ22'25''$ was mapped in the $J = 1 \rightarrow 0$ transitions of HCO^+, HCN, and CO with the 22 m ATNF Mopra telescope in three runs from 2004 June to September. The newly implemented on-the-fly (OTF) mode was used, in which the telescope takes data continuously while moving across the sky. Spectra were spaced by 7″ so that the 36″ Mopra beam (33″ at CO) would be well oversampled in the scanning direction; the row spacing was 10″, also oversampling the beam. Each row was preceded by an off-source integration at a location about 10′ from the map center. Typical SSB T^*_{sys} values of 200 K for HCO^+ and HCN and 600 K for CO were obtained in clear conditions. The pointing was checked on the SiO maser R Dor prior to each map; typical corrections were less than 5″. The digital correlator was configured to output 1024 channels across 64 MHz in each of two orthogonal polarizations, except for the 2004 June observations in which only one polarization was recorded. Initial spectral processing

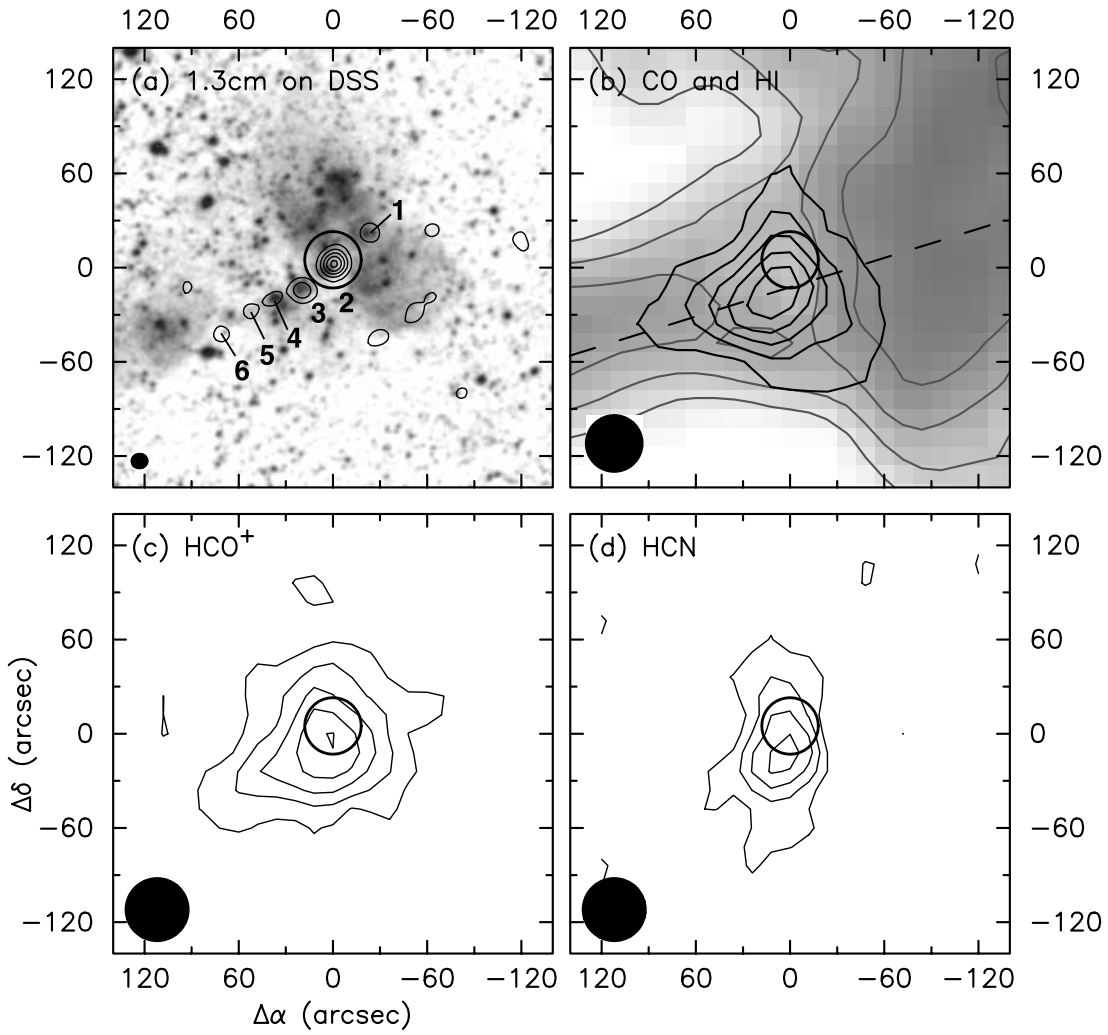

FIG. 2.—(*a*) ATCA 1.3 cm map (*contours*) overlaid on an *R*-band image from the Digitized Sky Survey. Contour levels correspond to $2n^2$ mJy beam^{-1} ($n = 1, 2, \ldots$). (*b*) Mopra CO (1–0) map (*black contours*) overlaid on an H I peak intensity image (*gray-scale and gray contours*). Contour levels are 7 K km s^{-1} for the CO map and 40, 50, . . . , 80 K for the H I map. The dashed line represents the position-velocity slice shown in Fig. 3. (*c*) Mopra HCO^+ (1–0) map. Contour levels are spaced by 0.6 K km s^{-1}. (*d*) Mopra HCN (1–0) map. Contour levels are spaced by 0.5 K km s^{-1}. In each case the open circle represents the ATCA pointing position. Offsets are relative to $\alpha_{J2000.0} = 5^h13^m18^s$, $\delta_{J2000.0} = -69^\circ22'25''$.

(baselining and calibration onto a T_A^* scale) was performed using the `livedata` task in AIPS++, and the spectra were gridded into data cubes using the AIPS++ `gridzilla` task. During the gridding, a Gaussian smoothing kernel with a FWHM half that of the beam size was convolved with the data, so the effective resolutions of the final cubes were 40″ for HCO^+ and HCN and 36″ for CO. The cubes were then rescaled onto a T_{MB} scale using an "extended beam" efficiency of $\eta_{xb} = 0.55$ for CO and 0.65 for HCO^+ and HCN (Ladd et al. 2005). This takes into account that sources larger than about 80″ in diameter will couple to both the main beam and the inner error beam of the telescope.

Comparison of Mopra and SEST spectra taken at the central Mopra position, with the Mopra maps convolved to the SEST resolution, indicate that the Mopra line intensities are lower by ∼30%. This is not surprising given that the extended beam efficiency is higher than the main beam efficiency η_{mb} by ∼30% (Ladd et al. 2005). While use of η_{mb} rather than η_{xb} would place the Mopra data on a more accurate temperature scale for compact sources, it would lead to an overestimate of the total map flux when assuming a Gaussian beam size equal to the main beam. Thus, we continue to use η_{xb} to calibrate the spectra, noting, however, that the quoted beam size is somewhat less than the effective beam size due to the presence of a significant inner error beam.

3. ANALYSIS AND RESULTS

3.1. *The N113 Molecular Cloud*

We begin by presenting maps and derived properties for the molecular cloud as a whole, based on the Mopra data. We discuss the high-resolution ATCA 3 mm data in § 3.2.

3.1.1. *ATCA* 1.3 cm *and Mopra Maps*

Figure 2*a* shows the ATCA 1.3 cm continuum image overlaid on a red Digitized Sky Survey image showing much of the diffuse Hα emission from the H II region. In addition to the string of three bright sources reported by Brooks & Whiteoak (1997), labeled 2, 3, and 4, we have detected three additional continuum sources along the same formation, one west of the main source (source 1) and two to the southeast (sources 5 and 6). The fluxes of the six continuum sources, from west to east, are estimated based on Gaussian fits to be 6.2, 66, 18, 4.1, 3.9, and 4.4 mJy. Measuring the flux by direct summation of image pixels yields

TABLE 2
PARAMETERS OF GAUSSIAN FITS TO MOPRA IMAGES

Line	Center R.A. (J2000.0)	Center Decl. (J2000.0)	Major Axis[a] (arcsec)	Minor Axis[a] (arcsec)	Position Angle (deg)
CO	5 13 19.9	−69 22 43	81 ± 2	67 ± 2	−80
HCO^+	5 13 19.4	−69 22 32	89 ± 3	67 ± 2	−59
HCN	5 13 19.3	−69 22 33	84 ± 4	25 ± 2	−4

NOTE.—Units of right ascension are hours, minutes, and seconds, and units of declination are degrees, arcminutes, and arcseconds.
[a] Deconvolved using a Gaussian beam of 36″ FWHM for CO and 40″ for HCO^+ and HCN.

fluxes consistent with these values within 1 mJy. Apparent sources that lie outside this linear structure (e.g., southwest of the image center) are likely to be sidelobes that were incompletely removed.

Figures 2*b*–2*d* show the Mopra CO, HCO^+, and HCN maps integrated from a velocity of 231 to 240 km s^{-1}. Remarkably, at the resolution of Mopra the molecular cloud appears to be a centrally condensed structure, in contrast to the filamentary structure that is characteristic of the H I clouds in the LMC (Kim et al. 2003). The CO map is shown overlaid on H I emission contours from the combined Parkes/ATCA survey (Kim et al. 2003). The HCO^+ emission imaged with Mopra shows a similar extent to the CO; however, the peak intensity is shifted ∼10″ to the north. The HCN emission appears to be narrower in the east–west direction than the other tracers, as confirmed by fitting of two-dimensional Gaussians to the images (Table 2).

3.1.2. *Mass and Dynamical Properties*

We can estimate the mass of the molecular cloud from the CO data in two ways. Adopting a conversion from kelvins to janskys of 1 K = 9.6×10^{-3} Jy $arcsec^{-2}$, the total CO (1–0) line flux detected by the Mopra observations is 2.9×10^3 Jy km s^{-1} over a $4' \times 4'$ region. Using a standard (Galactic) CO to H_2 conversion factor of $N_{H_2}/I_{CO} = 2.0 \times 10^{20}$ cm^{-2} (K km $s^{-1})^{-1}$ (Strong & Mattox 1996; Dame et al. 2001), this translates into a total gas mass (including He) of 8.2×10^4 $M_\odot$. We can compare this with a virial mass estimate, following Heikkilä et al. (1999), of $M_{vir} = 151 R_{CO} (\Delta v)^2$, where R_{CO} is the deconvolved FWHM size of the cloud in parsecs. For N113 a Gaussian fit to the integrated CO intensity gives $R = 74''$ (19 pc) after deconvolution, which for $\Delta v = 5.2$ km s^{-1} (the average FWHM line width over the inner $1' \times 1'$) yields $M_{vir} = 7.8 \times 10^4$ $M_\odot$. Although only a rough estimate, this suggests, as noted previously by Chin et al. (1997), that a standard conversion factor yields mass estimates for LMC molecular clouds that are consistent with virial mass estimates when observed at resolutions of ∼10 pc. A similar result was obtained for SMC clouds by Rubio et al. (1993).

Using the mass estimate above and a radius of 15 pc (estimated as 80% of the FWHM, following Heikkilä et al. 1999) gives an overall density for the cloud of $\langle n_H \rangle \sim 200$ cm^{-3}. This is significantly less than the critical density for excitation of HCO^+ and HCN (∼10^5 cm^{-3}), indicating that the material in the cloud is strongly clumped. Of course, our ATCA observations (described below) provide direct evidence of this clumping.

Inspection of the CO data cube reveals a velocity gradient of ∼5 km s^{-1} from the center to the southeast extension. The presence of such a gradient might be interpreted in terms of rotation (e.g., Rosolowsky et al. 2003). However, the CO position-velocity diagram (Fig. 3) is not strongly indicative of rotation but rather suggests a high velocity dispersion core that blends into a low velocity dispersion wing with a slightly different velocity centroid. We note that the wing emission could be composed of unresolved, clumpy structure. An overlapping slice through the H I data cube of Kim et al. (2003), smoothed to 1′ resolution, shows a similar velocity gradient across a filament-like structure 10′ (150 pc) in length. We conclude that the CO velocity gradient is not due to the rotation of a kinematically decoupled structure but instead reflects the bulk motion of the gas from which the molecular cloud formed.

The CO cloud appears to sit within a local minimum of H I peak brightness temperature (Fig. 2*b*). This does not necessarily require a large-scale conversion of the H I into H_2, as the H I at the location of the cloud still has a high integrated intensity. Rather, the lower peak T_b is mainly the result of a flat-topped line profile, which may indicate absorption by colder, optically thick H I.

3.2. *The Dense Embedded Clump*

3.2.1. *ATCA* 3 mm *Maps*

Figures 1*b*–1*f* show the integrated intensity maps for the four lines observed with ATCA, as well as the continuum at 86 GHz. Both the line and continuum emission appear to be concentrated in a single emission peak or "clump." These maps were produced by directly summing the velocity channels over the ranges given in Table 1. Because of the presence of large negative sidelobes in the maps, likely resulting from gain calibration errors and imperfect deconvolution, the integrated fluxes in Table 1 are given for both the inner $10'' \times 10''$ and $20'' \times 20''$ (larger values correspond to the smaller box) and should be considered

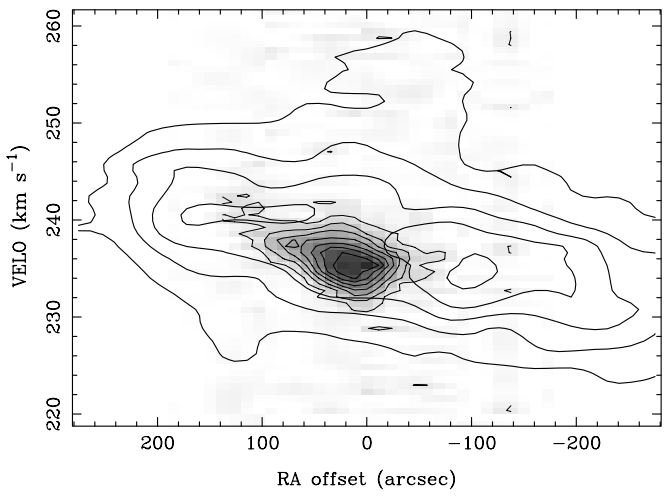

FIG. 3.—Position-velocity slice through the Mopra CO data cube (*gray scale with light contours*) with H I contours overlaid. The H I data have a resolution of 60″ FWHM. The slice is centered on $\alpha_{J2000.0} = 5^h13^m18^s$, $\delta_{J2000.0} = -69°22'43''$ and has a position angle of 107°. Contour levels are spaced by 0.5 K for CO and 15 K for H I.

TABLE 3
COMPARISON OF MOPRA AND ATCA FLUXES

Line (1)	Mopra (tot) (Jy km s^{-1}) (2)	Mopra (pb) (Jy km s^{-1}) (3)	ATCA (im) (Jy km s^{-1}) (4)	ATCA (u-v) (Jy km s^{-1}) (5)	$a_{\rm maj}$ (u-v) (arcsec) (6)	$a_{\rm min}$ (u-v) (arcsec) (7)
CO	2900	320	...	...	...	...
HCO^+	150	17	8.8 ± 0.2	14.2 ± 0.9	7.7 ± 0.8	5.4 ± 0.8
HCN	73	10	6.9 ± 0.2	10.5 ± 0.9	6.3 ± 2.2	4.8 ± 2.2
HNC	...	...	2.1 ± 0.1	3.9 ± 0.5	6.8 ± 3.0	5.2 ± 2.4
C_2H	...	...	1.5 ± 0.2	3.9 ± 1.1	7.0 ± 1.7	...
Cont.	...	...	42	47 ± 7	2.6 ± 0.6	...

NOTES.—All fluxes except continuum (which is in millijanskys) are in Jy km s^{-1}. Mopra fluxes are derived from the total image (col. [2]) and restricted to the ATCA field of view (col. [3]). ATCA fluxes are derived from the central $10'' \times 10''$ of the image and from a Gaussian fit to the visibility data. The Gaussian has been restricted to be circular for C_2H and the continuum.

indicative only. Also marked on each panel of Figure 1 are the positions of the obscured 2MASS point source 05131777−6922250 and the H_2O maser detected by Lazendic et al. (2002). Note that the infrared source coincides with the continuum source but is offset from the peak of the molecular line emission.

3.2.2. *Flux Recovered by ATCA*

Table 3 lists the total fluxes detected in the Mopra and ATCA maps, as well as the flux detected by Mopra with the ATCA primary beam response applied (i.e., the Mopra flux restricted to the ATCA field of view). We caution that the Mopra flux within a single primary beam may be overestimated if emission outside the beam is smoothed into it; it may also be underestimated because of the use of $\eta_{\rm xb}$ to calibrate the data. In any case, we find that the ATCA flux within the central $10'' \times 10''$ of the integrated HCO^+ and HCN maps is 50%–70% of the Mopra flux within the ATCA primary beam. For an independent comparison, we can also extrapolate the ATCA flux to short ("single-dish") baselines by fitting a two-dimensional Gaussian source in the visibility domain. As shown in the last three columns of Table 3, which give the fitted flux and FWHM major and minor axes, this yields a total flux that is consistent with the single-dish flux within the ATCA primary beam (assuming ~20% calibration uncertainties for both telescopes). The difference compared to measuring the flux in the image plane is likely due to a more inaccurate extrapolation to short baselines provided by CLEAN, coupled with uncorrected phase errors that lead to negative regions in the deconvolved images.

The analysis above suggests that the more extended component of HCO^+ or HCN emission that does not appear in the ATCA images can be inferred by inward extrapolation of the visibility amplitude. Assuming all of the flux is recovered by the visibility plane fitting, we derive an approximate beam-filling fraction (within the $36''$ ATCA beam) of 3% for the HCO^+ and HCN emission. Of course, this applies only to the region observed with the ATCA, which contains just ~12% of the total flux detected by Mopra. Clearly, it would be of great interest to cover the entire molecular cloud with an ATCA mosaic, to determine what fraction of the total line emission the interferometer would be sensitive to.

3.2.3. *Fitting of ATCA and SEST Spectra*

While the Mopra OTF maps of HCN and HCO^+ cover a larger area, their sensitivity at any given position is a factor of 3–4 worse than the pointed SEST spectra, so we have opted to derive line widths and hyperfine ratios from the SEST data for comparison with the ATCA data.

The averaged SEST spectra are shown in Figure 4, along with ATCA spectra taken through the central $1''$ pixel of each data cube. The HCO^+ and HCN brightness temperatures T_b measured in the ATCA maps are a factor of ~10 higher than the SEST measurements, which is not surprising given the presence of clumping and the factor of ~100 difference in beam area. We have also made single-component Gaussian fits to the HCO^+ spectra and three-component fits to the HCN spectra; the latter assume that the two satellite hyperfine transitions ($F = 0$–1 and 1–1) are separated by −7.07 and 4.85 km s^{-1} from the main component and have the same dispersion as the main component. We find for HCO^+ a FWHM line width (corrected for instrumental broadening) of 5.8 km s^{-1} for SEST and 5.5 km s^{-1} for ATCA. For HCN the line widths are 4.6 and 5.2 km s^{-1} for SEST and ATCA, respectively, although these are much more uncertain, being based on a multicomponent fit. We also find a velocity offset of −2.0 km s^{-1} in the ATCA HCN spectrum relative to SEST, which we attribute to limited spectral resolution and signal-to-noise ratio in the ATCA data.

The ratios between the hyperfine components of HCN can be used as a diagnostic of the optical depth, if LTE excitation is assumed (e.g., Fig. 2 in Harju 1989). In the optically thin case, the ratio of the $F = 0$–1/$F = 2$–1 transitions, referred to as R_{02}, should be 0.2; whereas the ratio of the $F = 1$–1/$F = 2$–1 transitions, referred to as R_{12}, should be 0.6. Fitting the SEST spectrum yields $R_{02} = 0.26 \pm 0.01$ and $R_{12} = 0.57 \pm 0.03$, where the errors are only the formal errors on the fit and thus a lower estimate. These appear consistent with optically thin emission. On the other hand, for the ATCA spectrum we find $R_{02} = 0.40 \pm 0.12$ and $R_{12} = 0.79 \pm 0.19$, indicating higher opacities for the dense clump at the 1–2 σ significance level (note, however, that *both* ratios are greater than their LTE values). While still requiring confirmation with higher spectral resolution data and/or observations of rare isotopomers, this suggests the presence of an optically thinner HCN component that dominates the total flux. We suggest that rather than constituting a truly diffuse interclump medium, this component is an enshrouding "clump envelope" that accounts for the difference between the fluxes measured in the ATCA images and those inferred by visibility fitting (Table 3).

3.2.4. *Clump Size and Line Width*

The visibility fits given in Table 3 indicate that the HCO^+ emission detected by the ATCA comes from a region $8'' \times 5''$ (2.0 pc × 1.3 pc) in size (FWHM), with the HCN emission coming from a somewhat smaller region. This implies a radius of ~1.6 pc, comparable to that of the largest clumps that are found

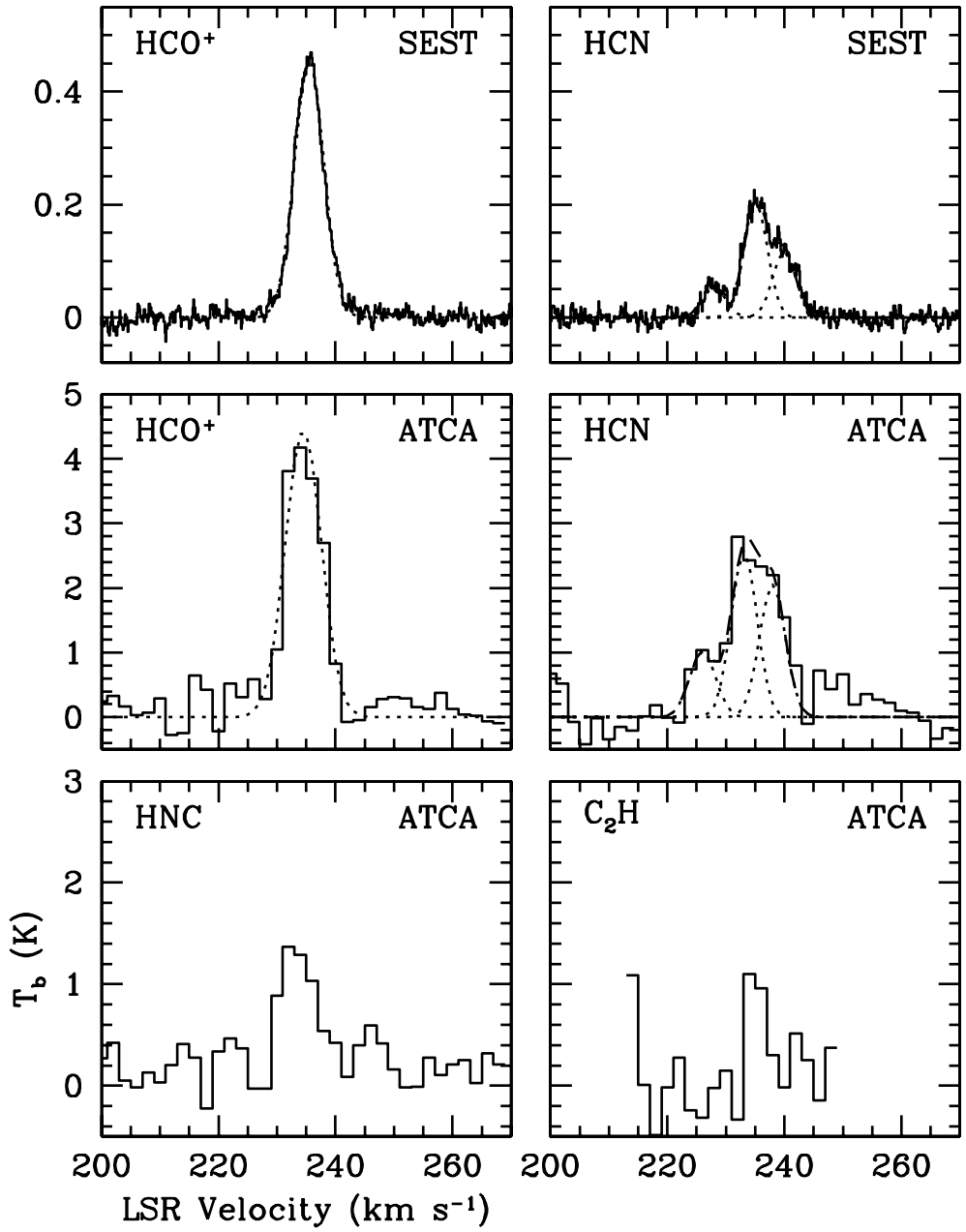

FIG. 4.—Comparison of ATCA and SEST spectra. SEST spectra, in T_{mb} units (*top two panels*), have been averaged over a $40'' \times 40''$ region centered on $\alpha_{J2000.0} = 5^h13^m18^s$, $\delta_{J2000.0} = -69°22'35''$. Spectra through the ATCA data cubes, smoothed to 2 km s^{-1} and converted to brightness temperature units using the synthesized beam size, have been taken at the nominal peak position of $\alpha_{J2000.0} = 5^h13^m17^s.2$, $\delta_{J2000.0} = -69°22'23''$. Gaussian fits to the HCO$^+$ and HCN lines (the latter taking into account the spacing of the three hyperfine components) are shown as dotted lines.

in Galactic massive star-forming regions (Mookerjea et al. 2004; Reid & Wilson 2005) and much larger than the typical size ($\sim$0.1 pc) of a core (a condensation that forms only a single star or a multiple star system). We therefore believe it is appropriate to refer to this object as a "clump." We note, however, that it is common in the literature (e.g., Plume et al. 1997) to use the term "massive cores" to refer to the birthplaces of the young stellar clusters where massive stars typically reside.

It is difficult to estimate the mass of the clump from the observed line fluxes, given considerable uncertainties in the excitation, abundances, and optical depths of HCO$^+$ and HCN. However, we can derive a virial mass as in § 3.1.2, this time using $R = 1.6$ pc and $\Delta v = 5.5$ km s^{-1}: $M_{vir} = 151R(\Delta v)^2 = 7.3 \times 10^3\ M_\odot$, or about 10% of the total cloud mass inferred from the CO data. Alternatively, Gao & Solomon (2004b) argue on the basis of large velocity gradient (LVG) calculations that the mass of dense gas traced by HCN satisfies

$$M_{dense}(H_2) \lesssim 25 \left(\frac{L_{HCN}}{1\ \mathrm{K\ km\ s^{-1}\ pc^{-2}}} \right) M_\odot .$$

They obtain this result assuming an HCN abundance of 2×10^{-8}, a kinetic temperature of 20–50 K, and an intrinsic HCN brightness temperature of $T_b > 5$ K. Using this formula gives an upper limit of $1.3 \times 10^4\ M_\odot$ for the N113 clump, within a factor of 2 of the virial estimate. The agreement between the two mass estimates, along with the high densities implied by the detection of HCN, HCO$^+$, and HNC, suggests that the assumption

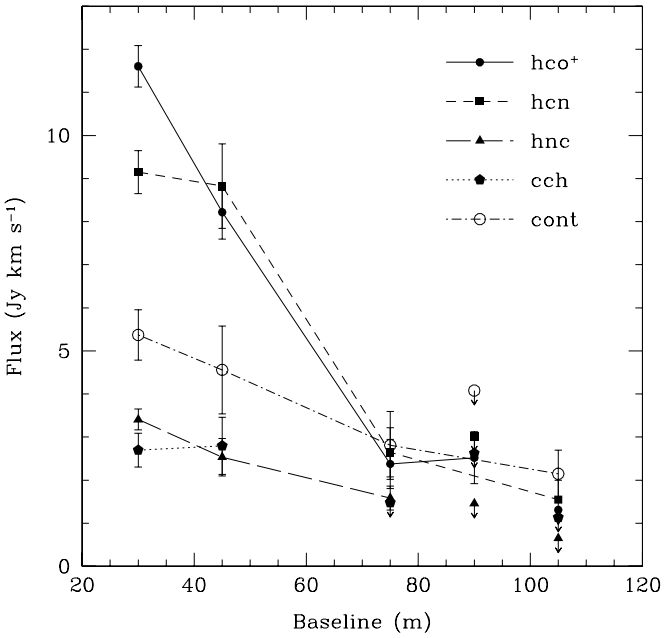

FIG. 5.—Integrated line flux for HCO^+, HCN, HNC, and C_2H as a function of projected ATCA baseline. Visibilities have been averaged within bins of 15 m width. For the continuum, fluxes are in units of 10 mJy. Plot symbols with arrows indicate 3 σ upper limits and are not connected with lines.

of virialization is reasonable. The average density of the clump is inferred to be $\langle n_{\rm H} \rangle \approx 10^5$ cm^{-3}, close to the critical densities for HCN and HCO^+.

3.2.5. *Line Ratio Analysis*

Figure 5 shows the integrated flux (in Jy km s^{-1}) for all four lines observed with ATCA as a function of the projected baseline. The equivalent curve for the continuum flux (in units of 10 mJy) is also shown. Since the ATCA spacings are roughly in multiples of 15 m, data have been averaged in bins of that width. As expected for a resolved source, the fluxes decrease on longer baselines, except for C_2H, which shows roughly equal fluxes on 30 and 45 m baselines (it is not detected on longer baselines, however). The relatively faster decline seen for HCO^+ compared to HCN is responsible for the larger source size inferred from the visibility fitting (Table 3) and is corroborated by the Mopra maps. For the shorter ATCA baselines, we have tabulated several integrated line ratios, $I(HCO^+)/I(HCN)$, $I(HCN)/I(HNC)$, and $I(C_2H)/I(HCN)$, in Table 4. These are given alongside the SEST line ratios reported by Chin et al. (1997). Note that for C_2H we only include the 87.3169 GHz line in these calculations.

4. DISCUSSION

4.1. *Comparison with Galactic Clumps*

Recently a number of papers have analyzed the substructure of molecular clouds hosting massive star formation in our Galaxy (e.g., Shirley et al. 2003; Faúndez et al. 2004). The clumps found in these studies have typical masses of 100–1000 $M_\odot$, sizes of 0.25–0.5 pc, and peak densities up to 10^6 cm^{-3}. The clump we have imaged in N113, with a radius $R \sim 1.6$ pc and mass $M \sim 10^4$ $M_\odot$, lies at the upper end of this distribution in terms of size and mass. We believe our size estimate to be realistic; while the resolution of the ATCA maps ($\sim 4''$) is only slightly smaller than the deconvolved size of the clump ($6''$), the visibility amplitude as a function of baseline indicates that the source is well resolved (Fig. 5). It is tempting to speculate that such massive clumps may be responsible for the formation of "populous" clusters of 10^3–10^4 stars in the LMC (van den Bergh 1991).

TABLE 4

INTEGRATED LINE INTENSITY RATIOS TOWARD THE N113 PEAK

Ratio	SEST[a]	ATCA 30 m	ATCA 45 m	ATCA 75 m
HCO^+/HCN.....	1.35 ± 0.06	1.27 ± 0.09	0.93 ± 0.13	0.90 ± 0.29
HCN/HNC	2.81 ± 0.21	2.68 ± 0.24	3.49 ± 0.71	1.67 ± 0.47
C_2H/HCN	0.29 ± 0.02	0.30 ± 0.05	0.32 ± 0.08	<0.56

[a] From Chin et al. (1997) .

Consistent with some previous studies of massive star-forming regions (e.g., Plume et al. 1997), we do not find evidence of a size–line width relation of the form $\Delta v \propto R^{0.5}$, as seen in low-mass star-forming regions (Larson 1981). Indeed, the velocity dispersion of the clump is comparable to or even larger than that of the molecular cloud as a whole (~ 5 km s^{-1}). This may indicate a high level of turbulence, as found in massive star-forming cores in the Galaxy. However, we caution that the observed line width could be affected by optical depth effects, and confirmation of this result with an optically thin tracer is required.

4.2. *The Star-forming Environment in N113*

The overall picture that emerges of the interstellar medium near N113 is of an environment that has been strongly affected by recent star formation. In addition to the diffuse Hα seen in optical images, the linear sequence of 1 cm continuum sources, including two that are associated with H_2O maser emission, point to the presence of young ionizing stars (Fig. 2*a*). The brightest H_2O maser is found near a relatively weak (~ 4 mJy) continuum source (source 4) southeast of the ATCA field, where there is still substantial HCO^+ and CO emission but no appreciable HCN. Moreover, referring to the 2MASS Point Source Catalog (Skrutskie et al. 2006), the associated near-infrared source is apparent in all three 2MASS bands ($m_J = 13.87$, $m_H = 13.46$, and $m_K = 12.71$), suggesting that it is relatively unobscured. These two lines of evidence point to an object that is somewhat more evolved than the brightest (~ 66 mJy) of the continuum sources, which is near the peak of the molecular line emission and detected in *K* band but not *J* band by 2MASS. This obscured source ($m_J > 14.97$, $m_H = 14.92$, and $m_K = 13.25$) is shown by a filled square in Figure 1. A third line of evidence is the presence of an OH maser in the former object, again suggesting a later stage of evolution.

Assuming the brightest continuum source (source 2) emits optically thin free-free emission (spectral index -0.1), the measured fluxes at 24 and 86 GHz (66 and 42 mJy, respectively) correspond to an ionizing photon output of $(1.5\text{–}3) \times 10^{49}$ s^{-1} (Condon 1992), equivalent to one or two O6 stars (e.g., Turner et al. 1998). Although the measured fluxes suggest a spectral index of -0.3 instead of -0.1, the larger calibration uncertainties of the 86 GHz data (a result of higher $T^*_{\rm sys}$ and relying on an SiO maser for gain calibration), possibly combined with resolving out some extended flux, could explain this discrepancy. The 86 GHz image also appears to show an elongation to the north, whose significance is unclear but is interesting in light of the presence of an H_2O maser $\sim 4''$ north of the *K*-band source. The maser and associated continuum emission could signify an outflow from the central ionizing source, but given their large projected distance from that source (~ 1 pc), are more likely to trace other ionizing stars in the same association.

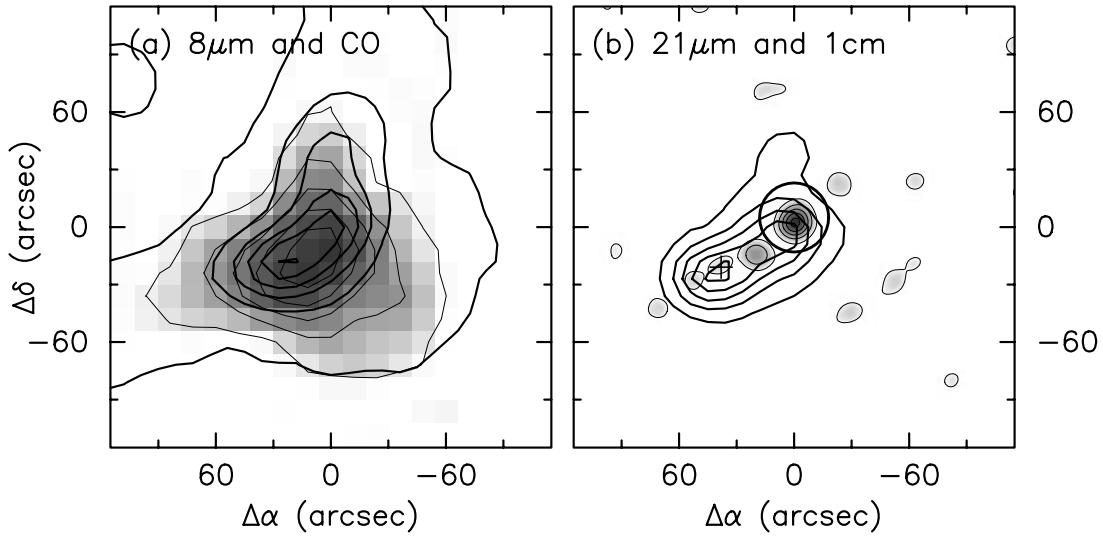

FIG. 6.—(*a*) 8 μm *MSX* image (*thick contours*) overlaid on the Mopra CO map from Fig. 2 (*thin contours and gray scale*). Contour levels for the *MSX* image are spaced by 1.5×10^{-10} W cm^{-2} sr^{-1}. (*b*) 21 μm *MSX* image (*thick contours*) overlaid on the 1 cm continuum map (*thin contours and gray scale*). Contour levels for the *MSX* image are spaced by 4×10^{-10} W cm^{-2} sr^{-1}, while the continuum image has contours of $2n^2$ mJy beam^{-1} ($n = 1, 2, \ldots$). The ATCA pointing position is shown as an open circle. The position of the bright H_2O maser is shown by a plus sign.

Regardless of the exact nature of the radio continuum emission, its location only 3.″6 (0.9 pc) from the dense molecular clump will surely affect the lifetime of the clump. One possibility is that the pressure of the expanding H II region may compress the clump and thereby incite gravitational collapse. Whitworth et al. (1994) discuss how shocked gas layers generated by expanding H II regions tend to fragment into $\sim 7\ M_\odot$ condensations that can become gravitationally unstable, yielding a self-propagating mode of star formation. Such a scenario might explain the alignment of star-forming regions seen in the continuum. On the other hand, Gorti & Hollenbach (2002) discuss how FUV radiation surrounding an H II region heats the clumpy molecular gas and eventually photoevaporates it, limiting the efficiency of star formation. A clump as massive as that inferred by our ATCA observations would not be easily photoevaporated but might initially experience a shock compression due to heating and expansion of its outer layers. Observations of shock tracers in this region with *Spitzer* may be able to directly trace this process and assess its ability to trigger new star formation.

4.3. *Evidence for PDR Chemistry*

The large HCO^+/HCN ratio observed with the shortest ATCA baseline (and in the Mopra data), and decreasing on longer interferometer baselines, is consistent with the HCO^+ emission originating from a more extended region than HCN. Similar conclusions for the LMC were reached by Johansson et al. (1994), based on SEST mapping of the N159W cloud, and Heikkilä et al. (1999), based on small maps of several additional clouds. As pointed out by Heikkilä et al. (1999), two of the major chemical pathways for the formation of HCO^+ involve C^+, which is expected to be abundant near the surfaces of clouds exposed to FUV radiation, i.e., in photon-dominated regions (PDRs). Thus, given the higher [C II]/CO flux ratios in the LMC (Mochizuki et al. 1994), and especially toward bright H II regions (Israel et al. 1996), HCO^+ emission likely traces lower density gas in the LMC in addition to well-shielded dense cores. The situation is less clear for HCN; while it can be produced by endothermic reactions between CN and H_2 in the outer layers of a PDR, it is easily be dissociated back to form CN in the presence of strong FUV radiation (Sternberg & Dalgarno 1995). We discussed above (§ 3.2.3) the possibility that the more optically thin HCN arises from a "clump envelope" that is not fully imaged in our ATCA data. The larger size of the HCO^+ emission region then implies a somewhat larger envelope in this line than in HCN.

C_2H is also expected to be enhanced when C^+ is enhanced and is especially strong relative to CO in the actively star-forming cloud N159W (Heikkilä et al. 1999). However, the SEST and ATCA observations show a roughly constant $I(C_2H)/I(HCN)$ from large to small scales, suggesting that C_2H may trace dense gas rather than the PDR region. Such a result is rather surprising, given the relatively low dipole moment of C_2H, which should lead to its excitation in even low-density regions. An alternative explanation is that C_2H appears less extended than HCO^+ because of lower optical depth. The hyperfine structure of C_2H ($N = 1{-}0, J = 3/2{-}1/2$) consists of two lines ($F = 2{-}1$ and $1{-}0$) separated by 12 MHz. The integrated intensity ratio of the 2–1 to 1–0 line measured by SEST is 1.8 (Chin et al. 1997), close to the theoretical value of 2 (Tucker et al. 1974) and indicating that the opacity is relatively low. On the other hand, the $HCO^+/H^{13}CO^+$ intensity ratio toward N113 as measured by SEST is 34 (Chin et al. 1996), consistent with the isotopic $^{12}C/^{13}C$ ratio derived by Johansson et al. (1994) for N159. Thus, the optical depth in HCO^+ is likely to be small as well. More sensitive observations will be needed to draw firmer conclusions on how C_2H is distributed relative to HCN and HCO^+.

A more direct indicator of PDR conditions may be the infrared emission at 8 μm, which is primarily attributed to large organic molecules known as polycyclic aromatic hydrocarbons (PAHs) heated by FUV radiation in the outer layers of the cloud. As Figure 6*a* indicates, the distribution of 6.8–10.8 μm emission near N113, as measured by the *Midcourse Space Experiment* (*MSX*) satellite (Price et al. 1998), closely matches the CO distribution in extent. This provides further evidence that the extended HCO^+ emission, which follows the CO distribution, is enhanced due to PDR chemistry. The 21 μm emission, which traces heated dust, is peaked slightly to the southeast of the PAH emission and corresponds well to the 1.3 cm radio continuum emission (Fig. 6*b*).

4.4. *Comparison of* HCN *and* HNC

Aside from a highly uncertain measurement for the 45 m baseline, the HCN/HNC intensity ratio appears to decrease on longer baselines, which sample smaller scale structure. This would confirm a prediction by Chin et al. (1997) that the ratio would be large in warm gas subject to strong UV heating, but approach unity in cloud cores. The difference may be due to additional neutral-neutral pathways for HCN formation that occur in a partially ionized medium, such as $CH_2 + N \rightarrow HCN + H$ (Goldsmith et al. 1981). These produce HCN faster than the equivalent reactions ($NH_n + C \rightarrow HNC + H_{n-1}$) produce HNC, due to the higher proportion of CH_n radicals and the tendency for C to be ionized in PDRs. However, the ability of such reactions to produce HCN/HNC abundance ratios much different from unity has been questioned (Herbst et al. 2000). In any case, the observed ratios are consistent with the HCN/HNC ratios of $\sim$1–6 observed in starburst galaxies (Aalto et al. 2002). A major uncertainty in interpreting intensity ratios as abundance ratios is the assumption of low optical depth. The decreasing HCN/HNC on small scales coincides with an apparent increase in the HCN opacity, which could affect the line profiles through saturation or self-absorption.

5. SUMMARY AND CONCLUSIONS

We have presented high-resolution imaging of HCO^+, HCN, HNC, and C_2H toward the N113 H II region in the LMC, performed with the ATCA interferometer, as well as single-dish mapping of the CO, HCO^+, and HCN lines with Mopra. Our main conclusions are summarized below.

1. On scales of several arcminutes, the molecular cloud ($M \sim 10^5\ M_\odot$) shows a weak velocity gradient that is shared with an H I filament that encompasses it. Several radio continuum sources lie along the center of the filament, making it the locus of recent star formation.

2. Near the brightest continuum source, which we interpret as a compact H II region, we detect a massive clump of dense molecular gas whose peak is slightly offset from the 3 mm continuum peak. The clump has a radius of $\sim$1 pc and, if in virial equilibrium, a mass of $\sim 10^4\ M_\odot$, about 10% of the cloud's mass. This would imply a density of $\sim 10^5$ cm^{-3}. With the ionizing flux of one or two O6 stars, the compact H II region may possibly trigger the formation of new stars in the clump.

3. While the clump (when combined with a more diffuse envelope inferred from visibility fitting) may account for most of the HCO^+ and HCN emission within the ATCA primary beam, the existence of additional clumps within the cloud is not excluded given the small extent of the region mapped thus far with the ATCA.

4. A decreasing HCO^+/HCN ratio on longer interferometer baselines, which probe smaller scales, suggests that the HCO^+ emanates in part from a more diffuse region than the HCN. This is consistent with the larger spatial extent of the HCO^+ emission in the Mopra map and its agreement with the CO and 8 μm morphology.

5. We also see evidence for a decrease in the HCN/HNC ratio on smaller scales. This may reflect a lower ratio in cold, dense regions, as found in the Galaxy, but the interpretation may be clouded by an increased opacity in the HCN line.

These observations demonstrate that maps of LMC molecular clouds on scales of a few parsecs can be used to investigate the internal structure and chemistry of clouds for comparison with Galactic samples. With the ATCA now covering a frequency range of 85–105 GHz with five antennas, further observations will soon achieve better sensitivity for a larger number of molecular lines, allowing for a more detailed comparison with PDR models. Ultimately, the ability to observe both low- and high-excitation lines at high resolution with the Atacama Large Millimeter Array will facilitate a comprehensive understanding of the properties of molecular clouds in an external galaxy.

We thank L. Staveley-Smith and S. Kim for providing the H I data cube used for comparison, and M. Burton and C. Henkel for providing helpful comments on the manuscript. Paul Ho and an anonymous referee also suggested improvements for the revised version. We thank R. Sault and the staff of the Narrabri observatory for assistance and troubleshooting at both ATCA and Mopra. The Mopra data were obtained in the University of New South Wales (UNSW) time allocation with the kind permission of M. Burton. T. W. acknowledges support from an ARC-CSIRO Linkage Postdoctoral Fellowship. Y. N. C. acknowledges financial support through National Science Council of Taiwan grant NSC 89-2119-M-032-001. This publication makes use of data products from the Two Micron All Sky Survey, which is a joint project of the University of Massachusetts and the Infrared Processing and Analysis Center/California Institute of Technology, funded by the National Aeronautics and Space Administration and the National Science Foundation. This research has made use of NASA's Astrophysics Data System Bibliographic Services. The Digitized Sky Surveys were produced at the Space Telescope Science Institute under US Government grant NAGW-2166.

Facilities: ATCA, Mopra, SEST

REFERENCES

Aalto, S., Polatidis, A. G., Hüttemeister, S., & Curran, S. J. 2002, A&A, 381, 783
Bica, E., Claria, J. J., & Dottori, H. 1992, AJ, 103, 1859
Blitz, L. 1991, in The Physics of Star Formation and Early Stellar Evolution, ed. C. J. Lada & N. D. Kylafis (Dordrecht: Kluwer), 3
Brooks, K. J., & Whiteoak, J. B. 1997, MNRAS, 291, 395
Chin, Y.-N., Henkel, C., Millar, T. J., Whiteoak, J. B., & Mauersberger, R. 1996, A&A, 312, L33
Chin, Y.-N., Henkel, C., Whiteoak, J. B., Millar, T. J., Hunt, M. R., & Lemme, C. 1997, A&A, 317, 548
Churchwell, E., Nash, A. G., & Walmsley, C. M. 1984, ApJ, 287, 681
Condon, J. J. 1992, ARA&A, 30, 575
Dame, T. M., Hartmann, D., & Thaddeus, P. 2001, ApJ, 547, 792
Faúndez, S., Bronfman, L., Garay, G., Chini, R., Nyman, L.-Å., & May, J. 2004, A&A, 426, 97
Gao, Y., & Solomon, P. M. 2004a, ApJ, 606, 271
———. 2004b, ApJS, 152, 63
Goldsmith, P. F., Langer, W. D., Ellder, J., Kollberg, E., & Irvine, W. 1981, ApJ, 249, 524
Gorti, U., & Hollenbach, D. 2002, ApJ, 573, 215
Graedel, T. E., Langer, W. D., & Frerking, M. A. 1982, ApJS, 48, 321
Harju, J. 1989, A&A, 219, 293
Heikkilä, A., Johansson, L. E. B., & Olofsson, H. 1999, A&A, 344, 817
Henize, K. G. 1956, ApJS, 2, 315
Herbst, E., Terzieva, R., & Talbi, D. 2000, MNRAS, 311, 869
Hirota, T., Yamamoto, S., Mikami, H., & Ohishi, M. 1998, ApJ, 503, 717
Huettemeister, S., Henkel, C., Mauersberger, R., Brouillet, N., Wiklind, T., & Millar, T. J. 1995, A&A, 295, 571
Israel, F. P., Maloney, P. R., Geis, N., Herrmann, F., Madden, S. C., Poglitsch, A., & Stacey, G. J. 1996, ApJ, 465, 738
Johansson, L. E. B., Olofsson, H., Hjalmarson, A., Gredel, R., & Black, J. H. 1994, A&A, 291, 89
Kim, S., Staveley-Smith, L., Dopita, M. A., Sault, R. J., Freeman, K. C., Lee, Y., & Chu, Y.-H. 2003, ApJS, 148, 473
Ladd, N., Purcell, C., Wong, T., & Robertson, S. 2005, Publ. Astron. Soc. Australia, 22, 62
Larson, R. B. 1981, MNRAS, 194, 809

Lazendic, J. S., Whiteoak, J. B., Klamer, I., Harbison, P. D., & Kuiper, T. B. H. 2002, MNRAS, 331, 969
Mochizuki, K., et al. 1994, ApJ, 430, L37
Mookerjea, B., Kramer, C., Nielbock, M., & Nyman, L.-Å. 2004, A&A, 426, 119
Panagia, N. 1999, in IAU Symp. 190, New Views of the Magellanic Clouds, ed. Y.-H. Chu (San Fransisco: ASP), 549
Plume, R., Jaffe, D. T., Evans, N. J., II, Martin-Pintado, J., & Gomez-Gonzalez, J. 1997, ApJ, 476, 730
Price, S. D., Tedesco, E. F., Cohen, M., Walker, R. G., Henry, R. C., Moshir, M., Paxton, L. J., & Witterborn, F. C. 1998, in IAU Symp. 179, New Horizons from Multi-Wavelength Sky Surveys, ed. B. J. McLean et al. (Dordrecht: Kluwer), 115
Reid, M. A., & Wilson, C. D. 2005, ApJ, 625, 891
Rosolowsky, E., Engargiola, G., Plambeck, R., & Blitz, L. 2003, ApJ, 599, 258
Rubio, M., Lequeux, J., & Boulanger, F. 1993, A&A, 271, 9
Sault, R. J., Teuben, P. J., & Wright, M. C. H. 1995, in ASP Conf. Ser. 77, Astronomical Data Analysis Software and Systems IV, ed. R. A. Shaw, H. E. Payne, & J. J. E. Hayes (San Francisco: ASP), 433
Schilke, P., Walmsley, C. M., Pineau Des Forêts, G., Roueff, E., Flower, D. R., & Guilloteau, S. 1992, A&A, 256, 595
Shirley, Y. L., Evans, N. J., II, Young, K. E., Knez, C., & Jaffe, D. T. 2003, ApJS, 149, 375
Skrutskie, M. F., et al. 2006, AJ, 131, 1163
Sternberg, A., & Dalgarno, A. 1995, ApJS, 99, 565
Strong, A. W., & Mattox, J. R. 1996, A&A, 308, L21
Tucker, K. D., Kutner, M. L., & Thaddeus, P. 1974, ApJ, 193, L115
Turner, J. L., Ho, P. T. P., & Beck, S. C. 1998, AJ, 116, 1212
van den Bergh, S. 1991, ApJ, 369, 1
Whiteoak, J. B., & Gardner, F. F. 1986, MNRAS, 222, 513
Whitworth, A. P., Bhattal, A. S., Chapman, S. J., Disney, M. J., & Turner, J. A. 1994, MNRAS, 268, 291